Discover the maze-like network for glabridin biosynthesis

Zhang *et al.*

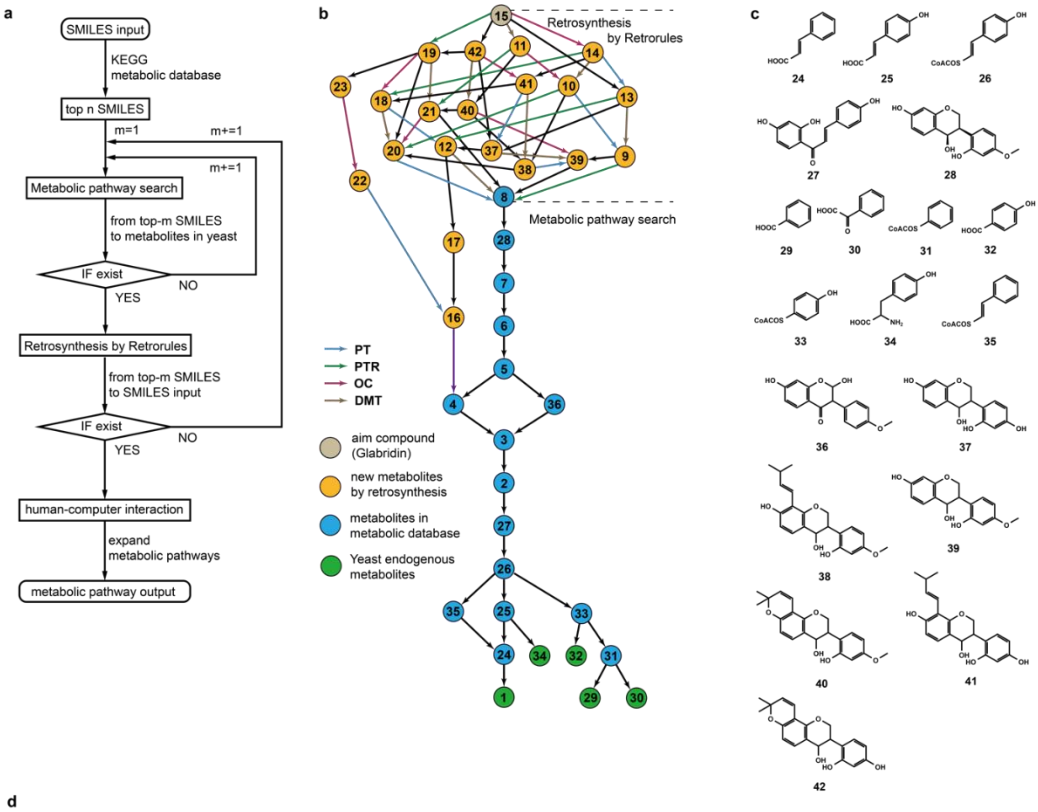

d

Pathway Index	Path	Steps
P1	2 3 4 16 22 23 19 15	7*
P2	2 3 4 16 17 12 13 14 15	8
P3	2 3 4 16 17 12 18 14 15	8
P4	2 3 4 16 17 12 18 19 15	8
P5	2 3 5 6 7 8 9 10 11 15	9
P6	2 3 5 6 7 8 9 10 14 15	9
P7	2 3 5 6 7 8 9 13 14 15	9
P8	2 3 5 6 7 8 12 13 14 15	9
P9	2 3 5 6 7 8 12 18 14 15	9
P10	2 3 5 6 7 8 12 18 19 15	9
P11	2 3 5 6 7 8 20 10 11 15	9
P12	2 3 5 6 7 8 20 10 14 15	9
P13	2 3 5 6 7 8 20 21 11 15	9

Supplementary Fig. 1. Retrobiosynthesis of glabridin. a) Retrobiosynthesis includes metabolic pathway exploration using established biological databases, and rule-based retrobiosynthesis analysis. b) Retrobiosynthesis network of Glabridin. c) Chemical structure in b. The algorithm predicted 58 distinct pathways connecting glabridin to medicarpin, along with 12 pathways linking medicarpin to yeast endogenous metabolites. These combined predictions yielded 696 potential glabridin biosynthesis routes. d) Summary of Retrobiosynthesis results for the glabridin. Blue nodes represent intermediate compounds, and the red node indicates the final product, glabridin. The 13 candidate pathways (P1-P13) were obtained by traversing the refined reaction subgraph in Fig. 1a, which was manually curated from the broader retrosynthesis-derived network in Supplementary Fig. 1b and further streamlined by retaining only intermediates endogenous to licorice. To avoid redundant branching of early branching, the conversion from 4 to 5 was omitted. *The path from compound **23** to compound **19** involves multiple reaction steps, with the actual step count exceeding 7.

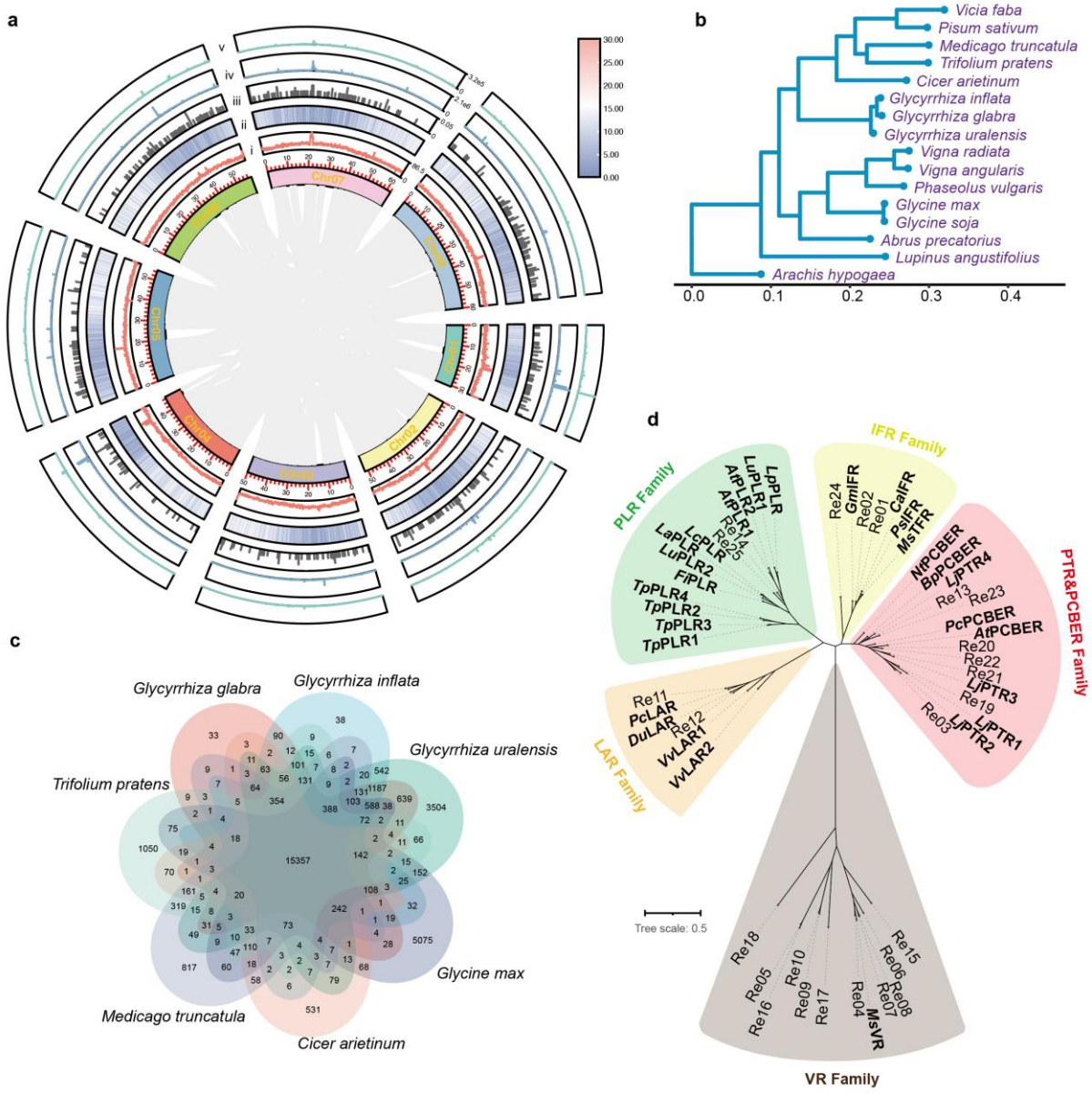

Supplementary Fig. 2. Assembly and phylogenic information of *G. glabra*. a) Sequencing information of a high-precision genomic assembly of *G. glabra*, circles stand for (i) GC ratio (%), (ii) gene density (genes/1e7 bp), (iii) N base ratio (%), (iv) coverage of Illumina sequencing, (v) coverage of PacBio sequencing. b) Phylogenic tree constructed with orthology genes of *G. glabra* and neighbor species in Leguminosae. c) Common and unique orthology groups owned by *G. glabra* and neighbor species. d) Phylogenetic analysis of newly discovered reductases in licorice was performed using previously reported plant-derived enzymes—LAR, PLR, IFR, PTR, PCBER, and VR—for annotation, which are indicated in bold font. Different colors represent different clusters. The sequences used in this analysis are listed in Supplementary Table 10. Source data are provided as a Source Data file.

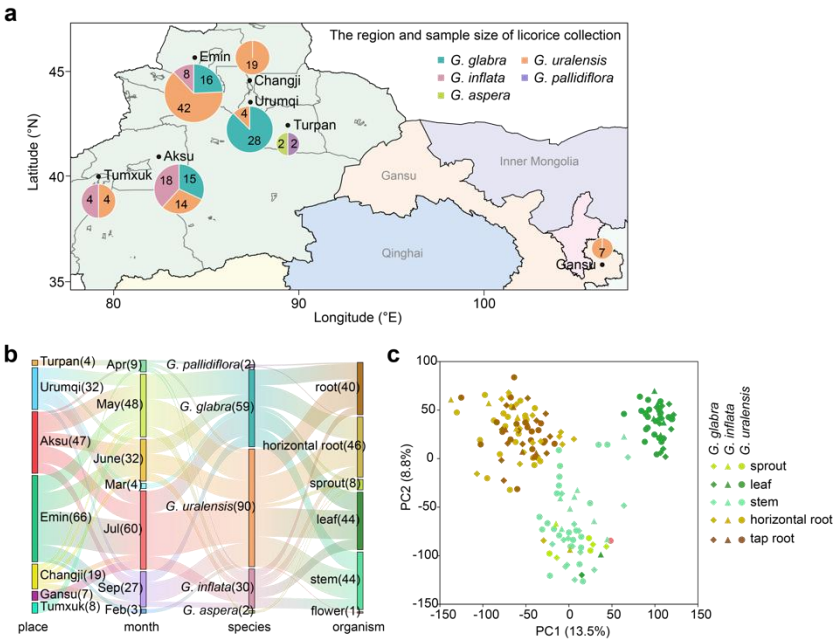

Supplementary Fig. 3. Transcriptomic analysis and sample collection of *Glycyrrhiza* species. a) Collection locations and species of *Glycyrrhiza* samples. b) Classification of the 183 *Glycyrrhiza* samples by location, collection month, species, and organ type. c) Clustering analysis of transcriptomes from *Glycyrrhiza* samples. Source data are provided as a Source Data file.

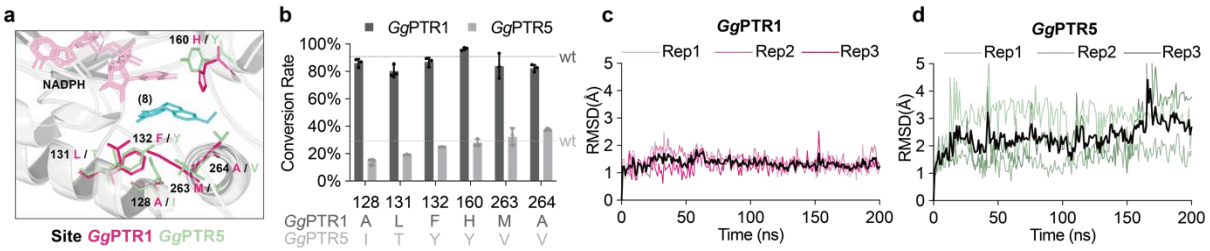

Supplementary Fig. 4. Functional and structural analysis of *Gg*PTR. a) Structural comparison of *Gg*PTR1 and *Gg*PTR5 highlighting the six divergent amino-acid sites surrounding the substrate-binding pocket. b) Conversion rates of *Gg*PTR1 and *Gg*PTR5 mutants generated by reciprocal residue swapping at positions 128, 131, 132, 160, 263 and 264, using 20 mg/L medicarpin (**8**) as the substrate to quantify the conversion to vestitol (**9**). The V264A mutation increased GgPTR5 activity by 27.5% but did not restore activity to the level of GgPTR1. Data are mean ± s.d. from three biological replicates. c-d) Molecular dynamics simulations of *Gg*PTR1 (**c**) and *Gg*PTR5 (**d**) showing backbone RMSD trajectories over 200 ns across three independent replicates, where the black line represents the averaged RMSD, illustrating stable binding of medicarpin in *Gg*PTR1 versus unstable binding in *Gg*PTR5. Source data are provided as a Source Data file.

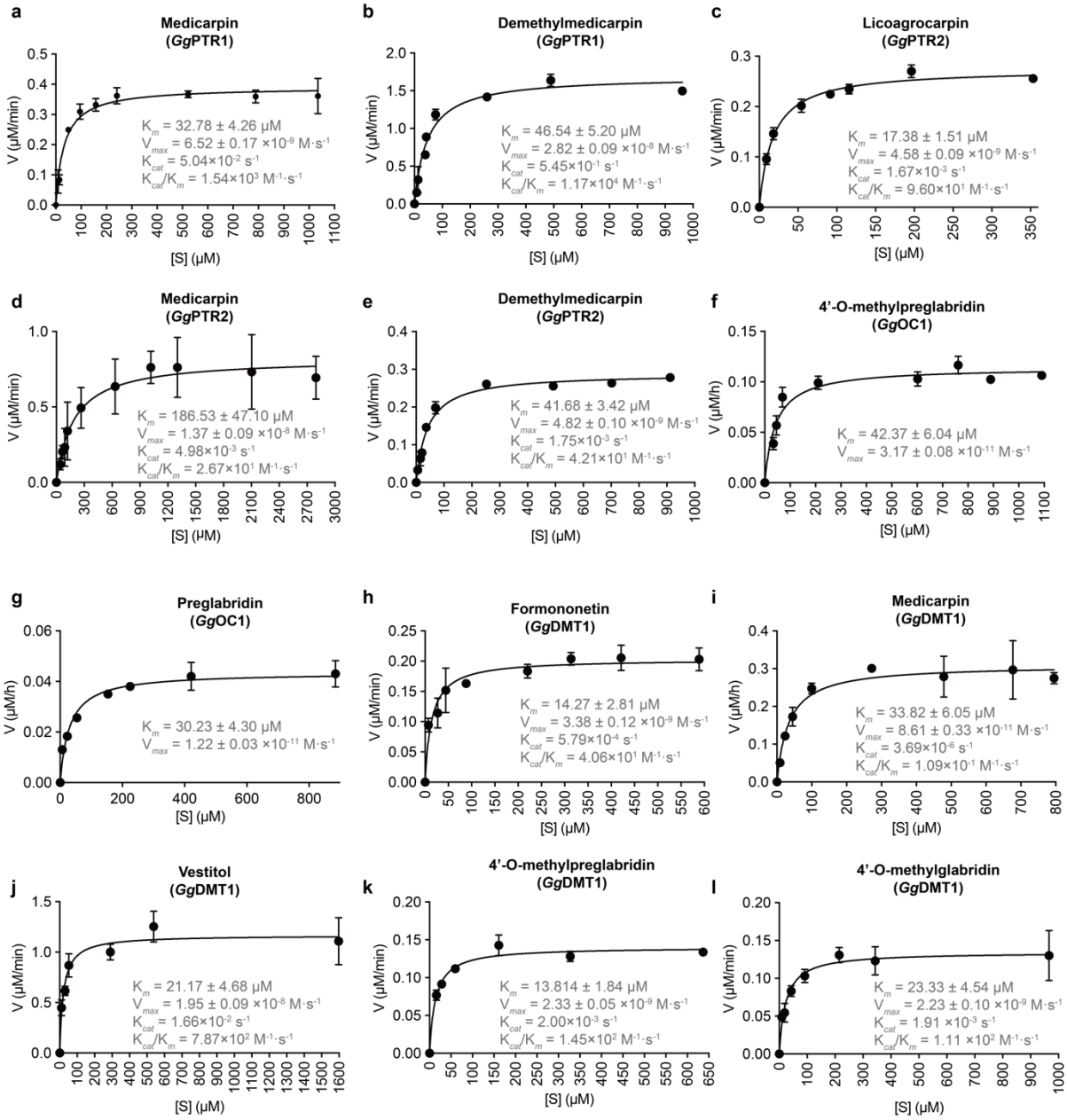

Supplementary Fig. 5. ***In vitro*** **enzyme activity.** Michaelis–Menten kinetic curves for purified recombinant enzymes *Gg*PTR1 (**a**, **b**), *Gg*PTR2 (**c**-**e**), *Gg*DMT1 (**h**–**l**), and for yeast microsomal preparations expressing *Gg*OC1 (**f**, **g**). Kinetic parameters (K_m, V_{max}, K_{cat}, and K_{cat}/K_m) were obtained by nonlinear regression fitting. Data represent mean ± s.d. from three independent biological replicates. Source data are provided as a Source Data file.

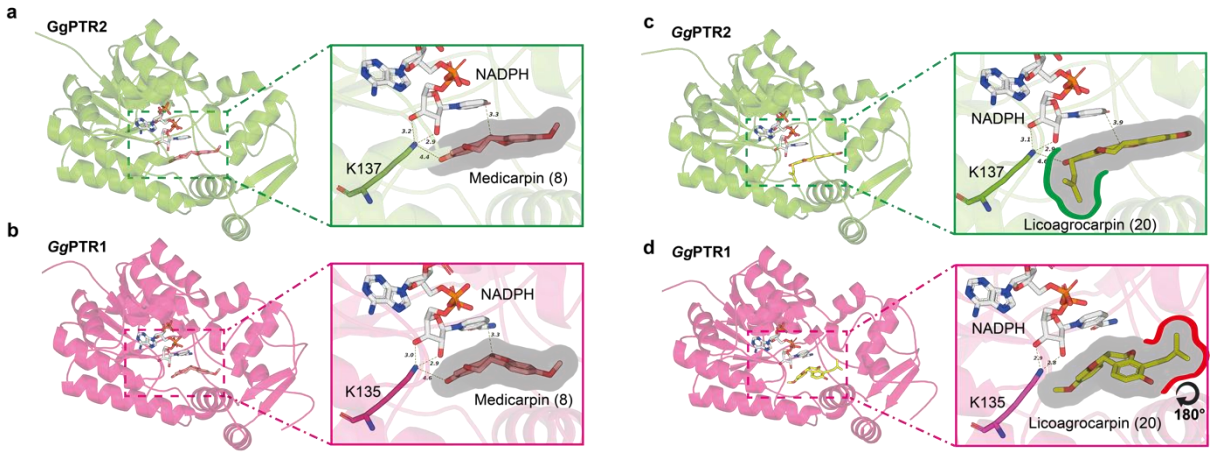

Supplementary Fig. 6. Molecular Docking Analysis of PTR–Substrate Interactions. Stereoview of the molecular docking results for substrate (**8**) in the active pocket of *Gg*PTR2 (a) and *Gg*PTR1 (b), and substrate (**20**) in the active pocket of *Gg*PTR2 (c) and *Gg*PTR1 (d). The size of the substrates is represented in surface mode. The docked substrate (**8**) or (**20**), cofactor NADPH, and catalytic lysine residues (K137 in *Gg*PTR2 and K135 in *Gg*PTR1) are depicted as sticks. The black dashed lines indicate the distances between substrate 7-OH and lysine, as well as the potential electron transfer from the NADPH hydrogen donor to the substrate carbon. The thick lines in c. and d. represent the isopentenyl group. The black arrow in d. indicates a 180° rotation of the substrate, which may result in inactivity of *Gg*PTR1 with (**20**). The cartoon representation of *Gg*PTR2 is shown in hot pink, and *Gg*PTR1 in light green. Substrate (**8**) is shown in salmon, and substrate (**20**) in yellow.

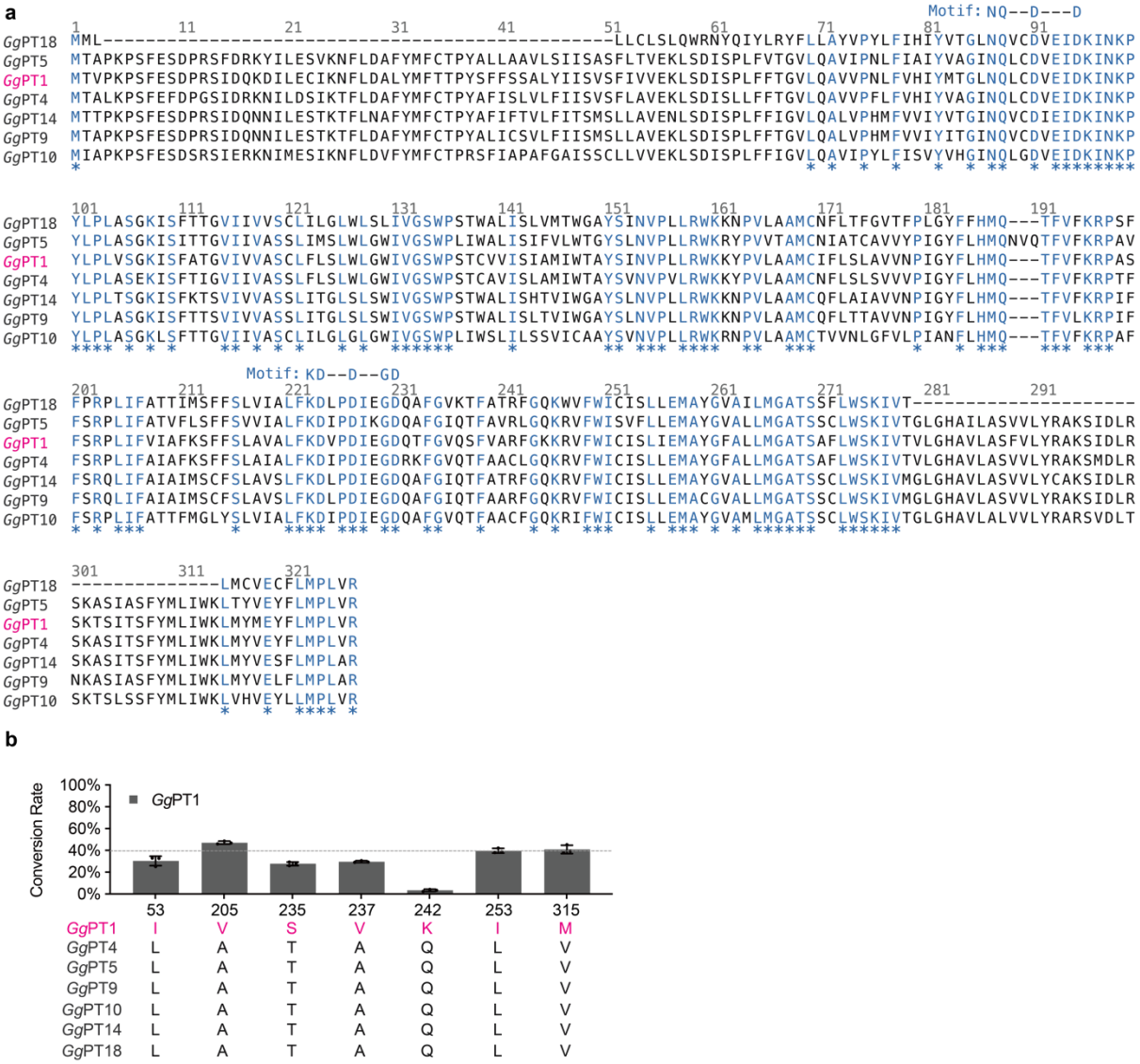

Supplementary Fig. 7. Functional and structural analysis of *Gg*PT1. a) Multiple sequence alignment of *Gg*PT1 with six non-functional PT homologs showing conserved motifs and the seven amino-acid residues uniquely present in *Gg*PT1. b) Conversion rates of *Gg*PT1 point mutants in which each residue was mutated to the consensus amino acid shared by the six PT homologs at positions where *Gg*PT1 uniquely differs, using 20 mg/L vestitol (**9**) as the substrate to measure the conversion to 4′-*O*-methylpreglabridin (**10**). Data represent mean ± s.d. from three biological replicates, and the marked loss of activity in the K242Q mutant identifies Lys242 as a key determinant of *Gg*PT1 catalytic function. Source data are provided as a Source Data file.

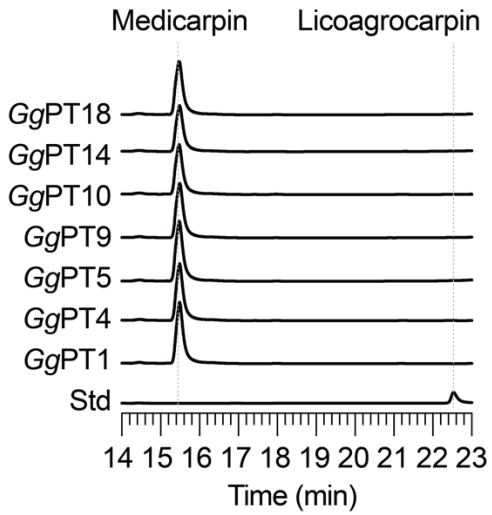

Supplementary Fig. 8. Functional validation of *Gg*PT homologs toward medicarpin. HPLC analysis of reactions catalyzed by *Gg*PT1 and six *Gg*PT homologs (*Gg*PT4, *Gg*PT5, *Gg*PT9, *Gg*PT10, *Gg*PT14, *Gg*PT18) with 20 mg/L medicarpin as the substrate. No detectable conversion or product formation was observed for any homolog, indicating that none of the tested *Gg*PTs catalyze prenylation of medicarpin. Source data are provided as a Source Data file.

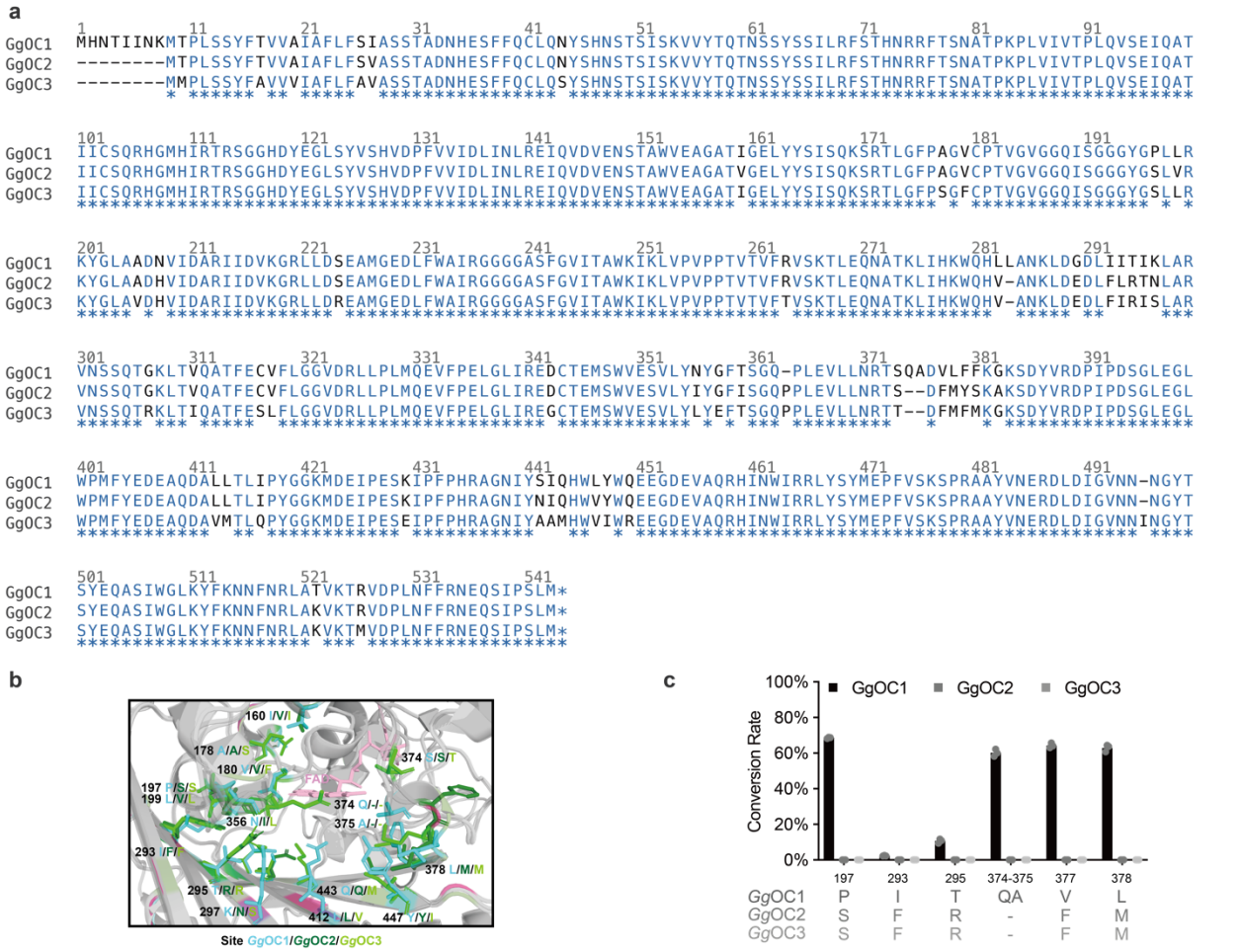

Supplementary Fig. 9. Sequence comparison and functional characterization of *Gg*OC mutations. a) Multiple sequence alignment of *Gg*OC1 with its two homologs *Gg*OC2 and *Gg*OC3 showing conserved regions and the extensive sequence divergence (>30 residues overall) in the two inactive homologs. b) Structural mapping of the active-site region highlighting more than 15 amino-acid differences between *Gg*OC1 and the two homologs. c) Conversion rates of *Gg*OC1 variants generated by substituting residues at the seven positions where both *Gg*OC2 and *Gg*OC3 carry conserved amino acids, using 10 mg/L 4′-*O*-methylpreglabridin (**10**) as the substrate to measure the conversion to 4′-*O*-methylglabridin (**11**). Data represent mean ± s.d. from three biological replicates; the I293F mutation nearly abolished activity and T295R markedly reduced activity, identifying these residues as critical determinants of oxidative cyclization. Source data are provided as a Source Data file.

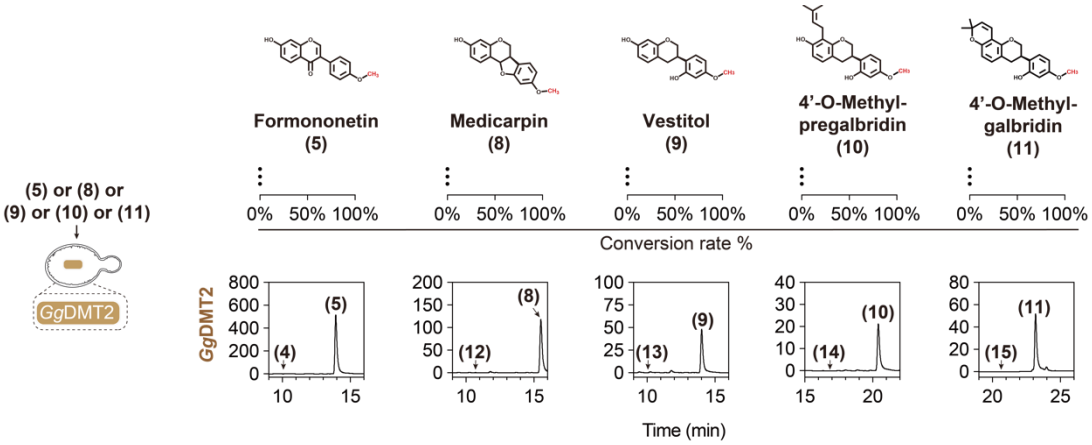

Supplementary Fig. 10. Characterization of *Gg*DMT2. HPLC analysis showing that *Gg*DMT2 exhibits no detectable O-demethylation activity toward any of the five methylated substrates formononetin (**5**), medicarpin (**8**), vestitol (**9**), 4′-*O*-methylpreglabridin (**10**), and 4′-*O*-methylgalbdrin (**11**). Substrate-feeding assays were performed using 20 mg L^{-1} of each compound. Data shown are presented as mean ± SD from n = 3 independent biological replicates. Source data are provided as a Source Data file.

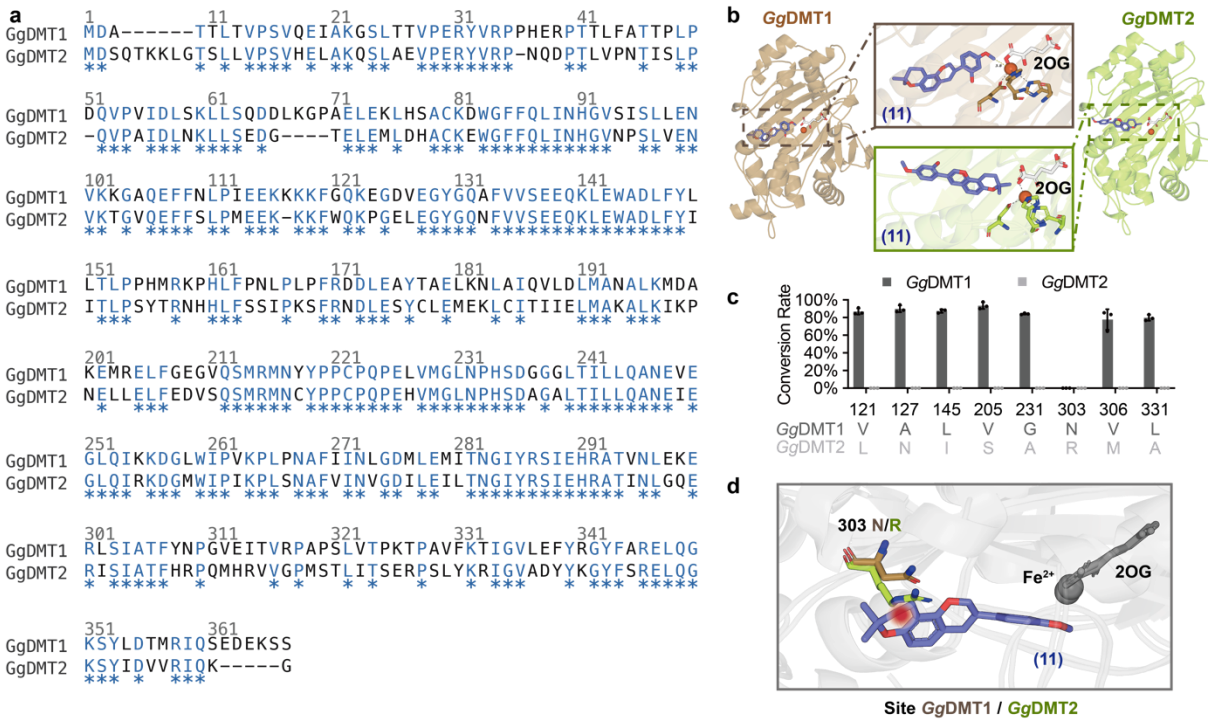

Supplementary Fig. 11. Sequence comparison and functional analysis of *Gg*DMT mutations. a) Sequence alignment of *Gg*DMT1 and *Gg*DMT2 showing extensive sequence divergence, with 138 amino-acid differences identified in total. b) Docking analysis of substrate 4′-*O*-methylglabridin (**11**) showing that it binds in an inverted orientation in *Gg*DMT2 compared with *Gg*DMT1. c) Conversion rates of *Gg*DMT1 and *Gg*DMT2 variants generated by substituting the eight divergent residues surrounding the predicted catalytic pocket, using 20 mg/L 4′-*O*-methylglabridin (**11**) as the substrate to measure the conversion to glabridin (**15**). The N303R substitution in *Gg*DMT1 abolishes catalytic activity. Data represent mean ± s.d. from three biological replicates. d) Structural view showing that Arg303 introduces steric hindrance near the active center, blocking proper substrate accommodation and explaining the loss of activity. Source data are provided as a Source Data file.

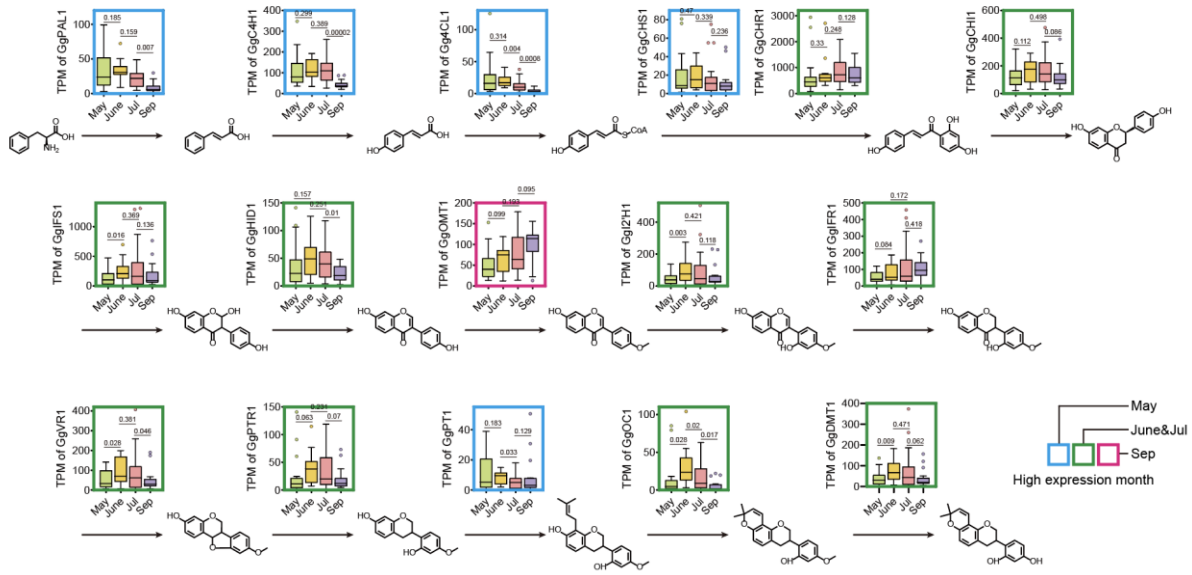

Supplementary Fig. 12. Monthly expression patterns of genes involved in glabridin biosynthesis in *Glycyrrhiza* roots. Samples collected in May, June, July, and September (n = 21, 14, 25, and 17, respectively) provide statistically meaningful representation. Gene expression profiles were grouped into three distinct temporal patterns: highest expression in May, June–July, or September. Box plots indicate the median (center line), first and third quartiles (box limits), whiskers extending to 1.5 × the interquartile range, and outliers shown as individual points. Statistical significance was assessed using a two-sided Student's *t*-test. Exact P values are shown in the figure. Source data are provided as a Source Data file.

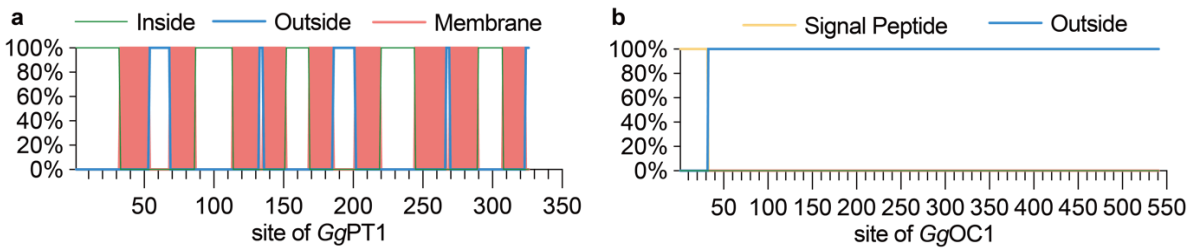

Supplementary Fig. 13. Transmembrane topology predictions of *Gg*PT1 and *Gg*OC1. a) Topology prediction of *Gg*PT1 using DeepTMHMM-1.0 showing nine predicted transmembrane helices, with alternating cytosolic (Inside), non-cytosolic (Outside), and membrane-embedded regions. b) Prediction for *Gg*OC1 indicating the presence of an N-terminal signal peptide and no additional transmembrane domains. Source data are provided as a Source Data file.

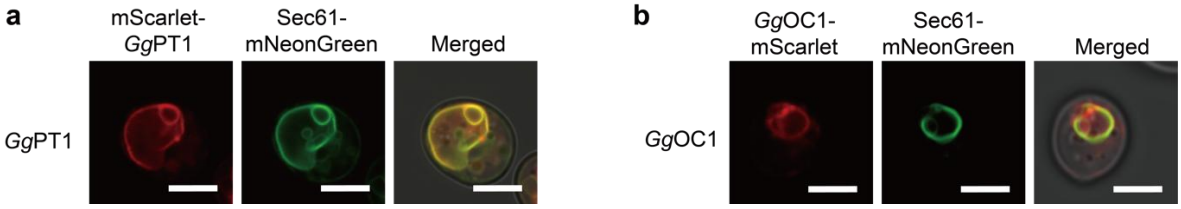

Supplementary Fig. 14. Yeast confocal microscopy. Confocal images of yeast cells expressing mScarlet-*Gg*PT1 (a) and *Gg*OC1-mScarlet (b), co-localized with the ER marker Sec61-mNeonGreen. Merged images show co-localization of the red and green signals, indicating ER localization. Scale bar, 5 μm.

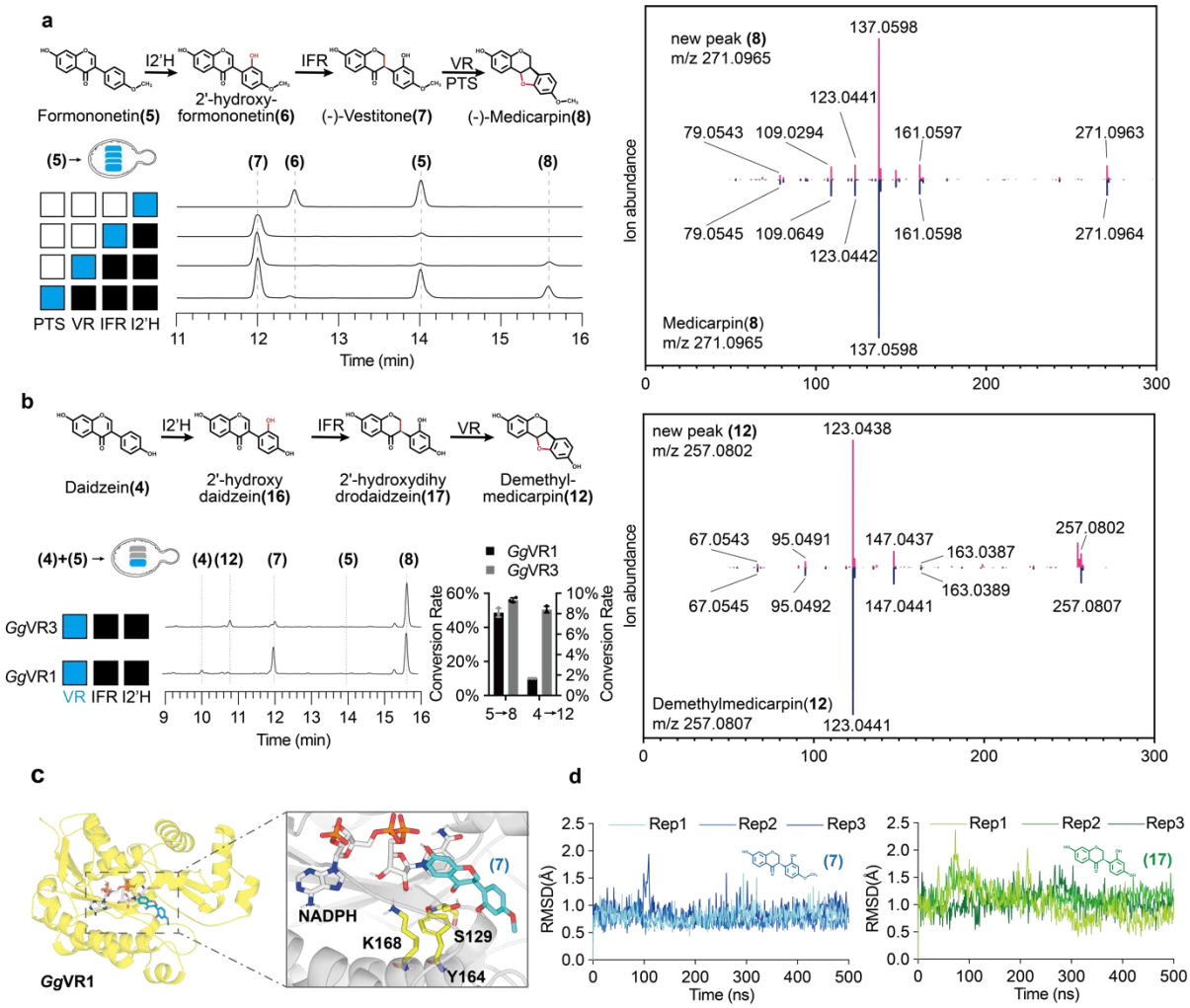

Supplementary Fig. 15. Stepwise reconstitution of the core scaffold biosynthesis of medicarpin and demethylmedicarpin in *S. cerevisiae*. a) Stepwise characterization of the *GgI2'H1–GgIFR1–GgVR1–GgPTS1* module in yeast with 50 mg/L of the methylated substrate formononetin (**5**). b) Functional characterization of *Gg*I2′H1–*Gg*IFR1 combined with different vestitone reductases (VRs) for the conversion of methylated (**5**) and unmethylated (**4**) substrates. Both *Gg*VR1 and *Gg*VR3 can convert 2′-hydroxydihy drodaidzein (**17**) to Demethylmedicarpin (**12**) without PTS, which is similar with previous reported THIS. Both formononetin (**5**) and daidzein (**4**) were supplied at 50 mg/L. Data shown are presented as mean ± SD from n = 3 independent biological replicates. c) The overall and local views of the protein-ligand-cofactor complex after 500 ns of molecular dynamics simulation. The catalytic triad residues (Ser-Tyr-Lys), depicted as sticks, potentially facilitate catalysis. d) RMSD profiles of ligands (**7**, blue; **17**, green) fitted to the protein backbone. **7** maintains consistent proximity, whereas **17** exhibits fluctuations, adversely affecting the reduction reaction. Source data are provided as a Source Data file.

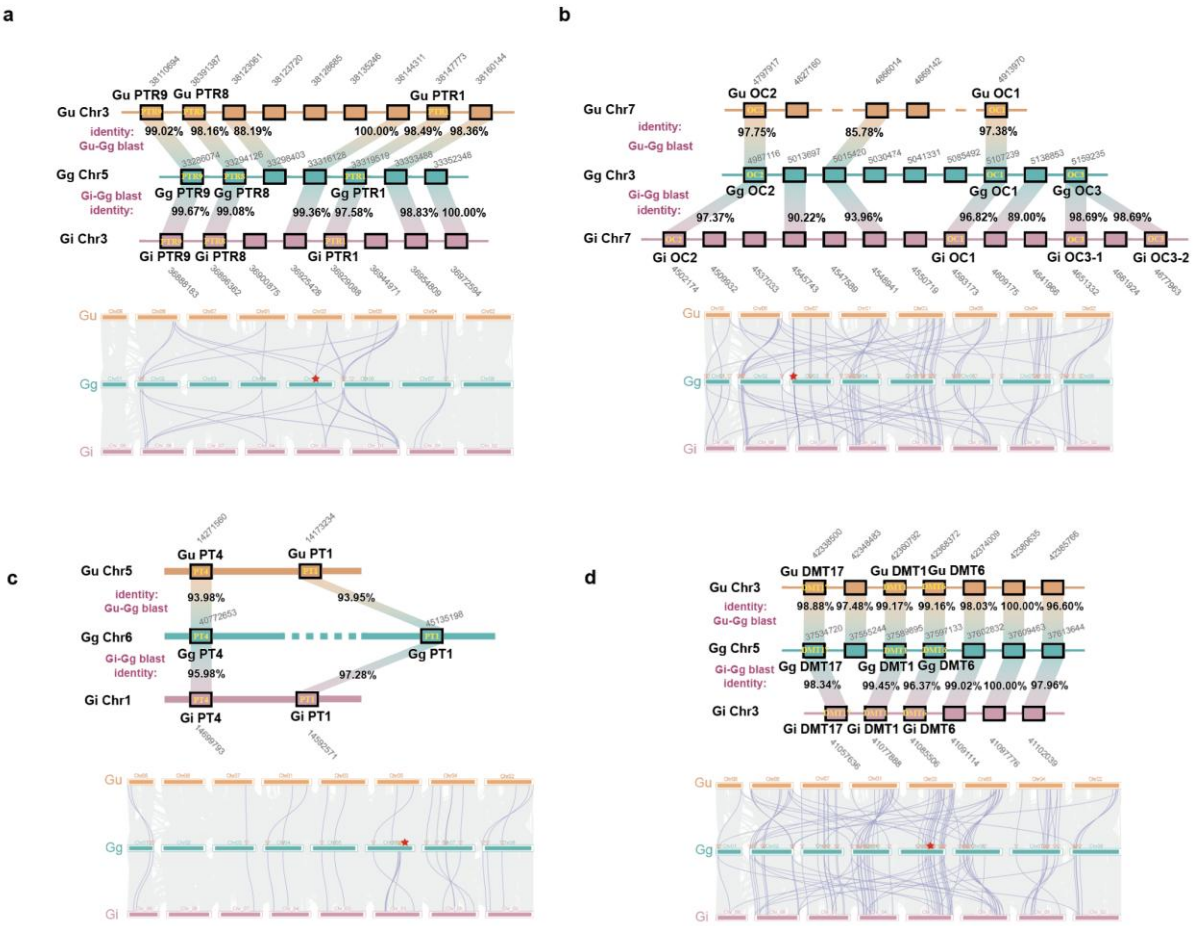

Supplementary Fig. 16. Cross-species analysis of tailoring enzymes in *Glycyrrhiza*. Locations of target genes in the *G. glabra*, *G. inflata*, and *G. uralensis* genomes and their corresponding evolutionary relationships. Based on protein similarity and phylogenetic relationships of adjacent gene proteins, the corresponding genomic locations and protein sequences of *Gg*PTR1 (a), *Gg*OC1 (b), *Gg*PT1 (c), and *Gg*DMT1 (d) in *G. inflata* and *G. uralensis* were identified (Supplementary Data 4).

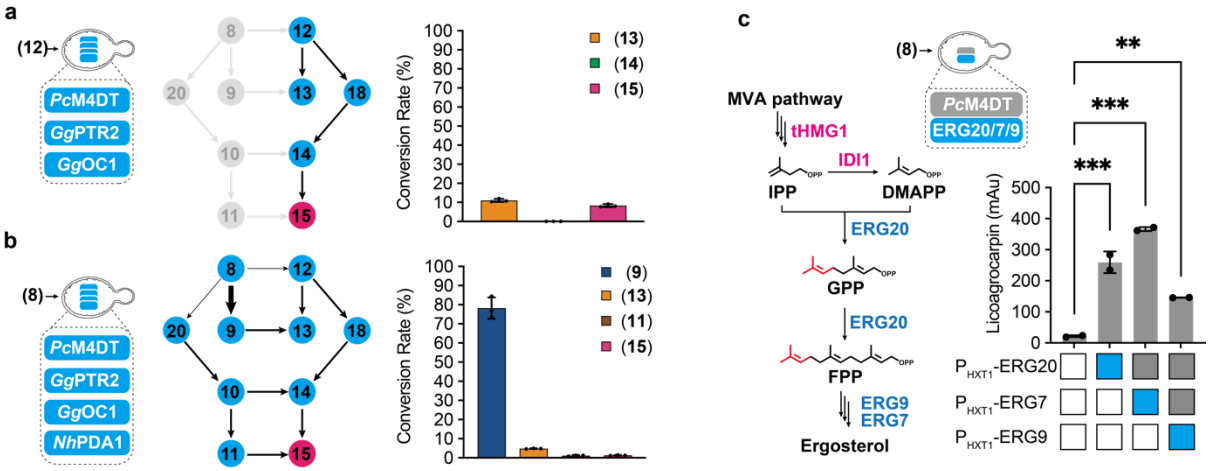

Supplementary Fig. 17. Reconstitution of the glabridin biosynthetic pathway (PTR–PT–OC–DMT) in *S. cerevisiae*. a) Characterization of *Pc*M4DT-*Gg*PTR2-*Gg*OC1 module in yeast. 7.2 mg/L substrate (**12**) was fed. b) Characterization of *Pc*M4DT-*Gg*PTR2-*Gg*OC1-*Nh*PDA1 module in yeast. 20 mg/L substrate (**8**) was fed. c) Combinatorial repression of downstream enzymes in the mevalonate (MVA) pathway (*ERG20*, *ERG9*, and *ERG7*) was implemented to relieve prenylation bottlenecks. Data shown in (a-c) are presented as mean ± SD from n = 3 independent biological replicates. Source data are provided as a Source Data file.

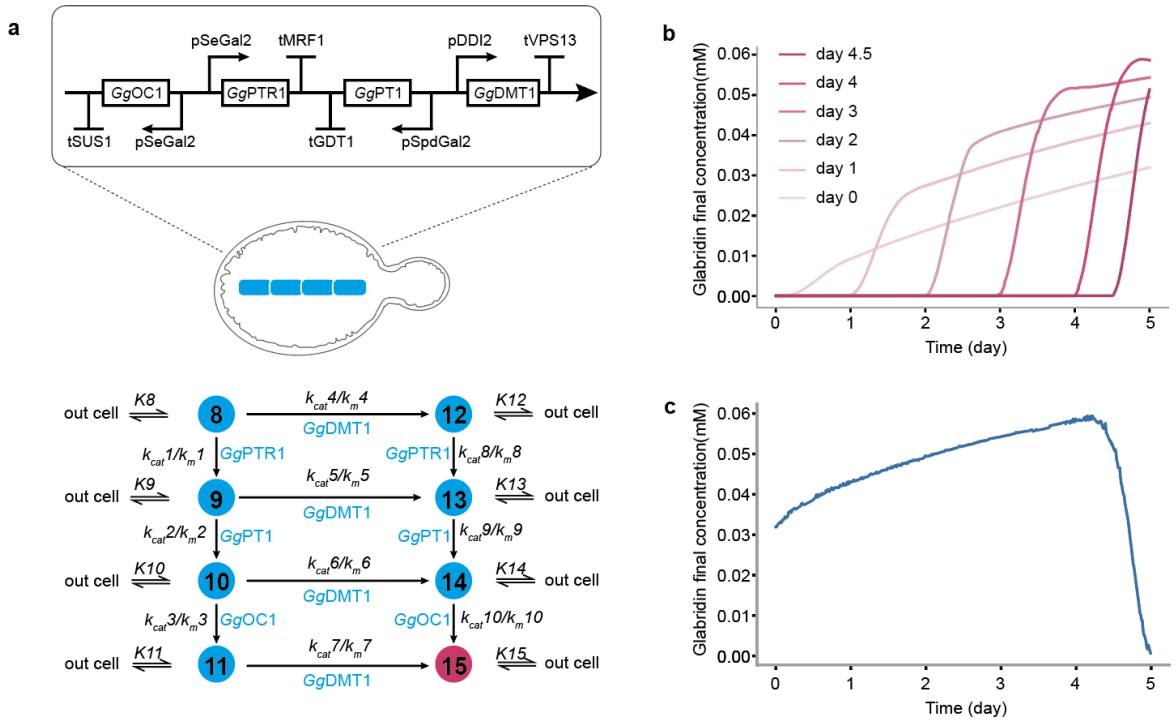

Supplementary Fig. 18. Metabolic flux modelling of glabridin concentration dynamics via under induced expression of *Gg*DMT1. a) Metabolic reaction network and parameters. b) Glabridin production dynamics under different initial induction timing. c) Final glabridin concentration versus *Gg*DMT1 induction timing under a fixed 5-day fermentation duration. When *Gg*DMT1 was induced before day 4, later induction times resulted in higher final glabridin concentrations. Induction after day 4 led to reduced final product concentrations due to insufficient catalytic reaction time and incomplete enzyme accumulation. Source data are provided as a Source Data file.

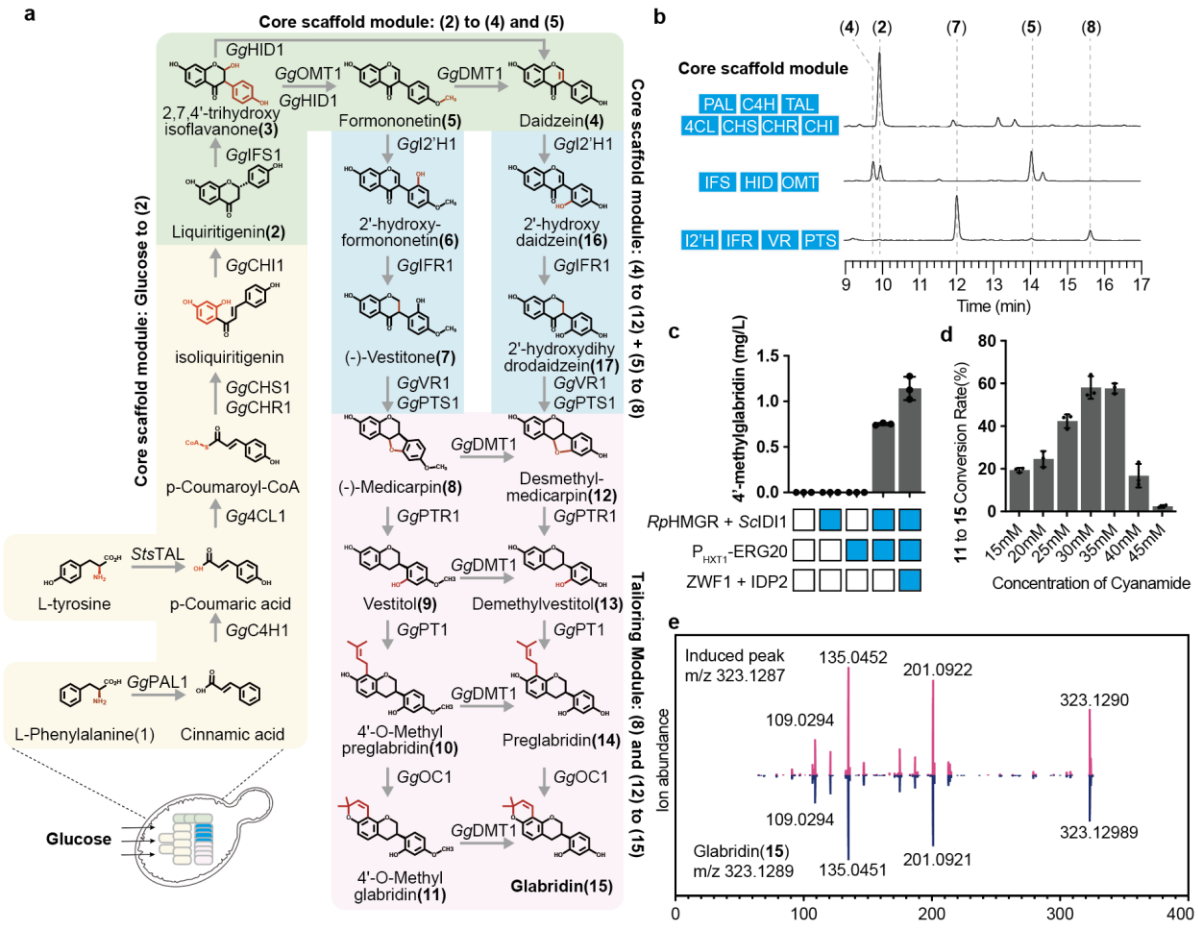

Supplementary Fig. 19. Modular design and validation of the *de novo* biosynthetic pathway for glabridin in *S. cerevisiae*. a) The glabridin biosynthetic pathway was divided into two modules: a core scaffold module converting glucose to medicarpin (**8**) and demethylmedicarpin (**12**), and a tailoring module converting (**8**) and (**12**) to glabridin (**15**). b) Functional validation of core scaffold module in yeast. c) Metabolic engineering to overcome bottlenecks in glabridin biosynthesis. d) Cyanamide-inducible expression of demethylase under the *DDI2* promoter in yeast. Yeast strains were supplemented with 12.5 mg/L 4′-*O*-methylglabridin (**11**) and various concentrations of cyanamide. e) Demethylation of *de novo* biosynthesized 4′-*O*-methylglabridin (**11**) to glabridin (**15**) in yeast. The identity of (**15**) was confirmed by LC–MS/MS analysis. Data shown in (c-d) are presented as mean ± SD from n = 3 independent biological replicates. Source data are provided as a Source Data file.

Supplementary Table 1. Functional annotation and classification of candidate genes.

Gene	Annotation	Total number
PAL	phenylalanine ammonia-lyase	3
C4H	trans-cinnamate 4-monooxygenase; Cinnamate 4-hydroxylase	3
4CL	4-coumarate:CoA ligase	6
CHS	chalcone synthase	4
CHR	NAD(P)H-dependent 6'-deoxychalcone synthase	4
CHI	chalcone-flavonone isomerase	3
IFS	2-hydroxyisoflavanone synthase	1
HID	2-hydroxyisoflavanone dehydratase	3
OMT	Isoflavone 4'-*O*-methyltransferase	2
I2'H	isoflavone 2'-hydroxylase	5
IFR	isoflavone reductase	3
VR	vestitone reductase; anthocyanidin reductase; dihydroflavonol 4-reductase	11
PTS	pterocarpan synthase	3
PTR	pterocarpin reductase; phenylcoumaran benzylic ether reductase; isoflavone reductase-like	7
PT	homogentisate phytyltransferase; glycinol 4-dimethylallyltransferase	18
OC	berberine bridge enzyme(BBE); cannabidiolic acid synthase; CYP71D; CYP82A; CYP736	39
DMT	Fe2OG dioxygenase (ODD); oxoglutarate/iron-dependent dioxygenase	6

Supplementary Table 2. Statistics of the number of differential amino acids between PT candidates and GgPT1.

Candidate	Number
GgPT4	53
GgPT9	75
GgPT14	78
GgPT5	85
GgPT10	96
GgPT18	157

Supplementary Table 3. Coexpression ranking of validated genes.

Subject	*GgIFS1*	*GgI2'H1*	*GgIFR1*	*GgVR1*	*GgPTR1*	*GgPT1*	*GgOC1*
GgIFS1	1	36	784	2	64	1139	183
GgI2'H1	13	1	10090	98	16	61	74
GgIFR1	158	3149	1	44	797	3946	1341
GgVR1	3	72	33	1	48	834	102
GgPTR1	88	20	8747	73	1	1980	2
GgPT1	2855	31	10004	2157	458	1	463
GgOC1	3574	272	13425	1704	2	3925	1

Supplementary Table 4. Statistics of the number of differential amino acids between GgOC2/GgOC3 and GgOC1.

Type	Gene	Number	In common
Multiple sequence align	*GgOC2*	34	
			15
Multiple sequence align	*GgOC3*	54	
Active sites	*GgOC2*	15	
			7
Active sites	*GgOC3*	20	

Supplementary Table 5. Reported genes.

Name	Source	GenBank
PcM4DT	*Cullen corylifolium*	AYV64464.1
MaDA1	*Morus alba*	UJH93677.1
MaDS1	*Morus alba*	WDV17865.1
MaOC1	*Morus alba*	WDV17872.1
FoPDA1	*Fusarium oxysporum* f. sp. *pisi*	AAR32716.1
NhPDA1	*Fusarium vanettenii* 77-13-4	XP_003044225.1
CYP80G2	*Coptis japonica*	A8CDR5.1
DMT734	*Bifidobacterium breve*	WP_016463155.1
ObF7ODM1	*Ocimum basilicum*	A0A0B6CGH9.1
PsCODM	*Papaver somniferum*	NP_001413550.1
PsDIOX2	*Papaver somniferum*	NP_001413560.1
PsT6ODM	*Papaver somniferum*	ADD85329.1
StsTAL	*Streptomyces* sp. NRRL F-4489	WP_199836185.1
RpHMGR	*Ruegeria pomeroyi*	WP_011241944.1
GuCPR3	*Glycyrrhiza uralensis*	AUG98241.1

Supplementary Table 6. Chemicals.

Chemical	CAS #	Source supplier	Catalog #
Daidzein	486-66-8	YuanYe Biotechnology Co., Ltd. (Shanghai, China)	A10158
Liquiritigenin	578-86-9	YuanYe Biotechnology Co., Ltd. (Shanghai, China)	V36471
Formononetin	485-72-3	YuanYe Biotechnology Co., Ltd. (Shanghai, China)	B20836
Demethylvestitol	65332-45-8	YuanYe Biotechnology Co., Ltd. (Shanghai, China)	B31038
Demethylmedicarpin	105815-70-1	Produced in *S. cerevisiae* expressing *Nh*PDA1 with exogenous medicarpin as substrate	this study
Vestitol	35878-41-2	YuanYe Biotechnology Co., Ltd. (Shanghai, China)	B30370
Medicarpin	32383-76-9	YuanYe Biotechnology Co., Ltd. (Shanghai, China)	B50633
Preglabridin	-	TargetMol (Boston, MA, USA)	T129460
Licoagrocarpin	202815-29-0	Produced in *S. cerevisiae* expressing *Pc*M4DT with exogenous medicarpin as substrate	this study
4'-*O*-methylpreglabridin	-	Acme Biopharma Co., Ltd. (Shanghai, China)	Chemical synthesis
4'-*O*-methylglabridin	105119-61-7	Acme Biopharma Co., Ltd. (Shanghai, China)	Chemical synthesis
Glabridin	59870-68-7	YuanYe Biotechnology Co., Ltd. (Shanghai, China)	B20474

Supplementary Table 7. Plasmids.

Plasmid	Genotype or characteristic	Reference
pgRNA-P_{ERG20}	*G418, 2μm, Amp^R, gRNA-P_{ERG20}*	This study
pgRNA-int2	*URA3, 2μm, Amp^R, gRNA-int2*	[1]
pgRNA-int5	*LEU2, 2μm, Amp^R, gRNA-int5*	[1]
pgRNA-int6	*LYS2, 2μm, Amp^R, gRNA-int6*	[1]
pgRNA-int7	*URA3, 2μm, Amp^R, gRNA-int7*	[1]
pgRNA-int16-int17	*HIS3, 2μm, Amp^R, gRNA-int16-int17*	[1]
pgRNA-int21	*URA3, 2μm, Amp^R, gRNA-int21*	[1]
pgRNA-Gal80	*URA3, 2μm, Amp^R, gRNA-Gal80*	[2]
pgRNA-MYTint1-Gal80	*URA3, 2μm, Amp^R, gRNA-MYTint1-Gal80*	[2]
pgRNA-MYTint4	*URA3, 2μm, Amp^R, gRNA-MYTint4*	[2]
pgRNA-MYTint5	URA3, 2μm, AmpR, gRNA-MYTint5	[2]

Supplementary Table 8. Strains.

Strain	Parent strain	Genotype	Note
BY4742		MATα his3Δ1 leu2Δ0 lys2Δ0 ura3Δ0	Wild-type strain
G01	BY4742	Gal80Δ0; MYTint1::pTPI1-GuCPR3	Knockout Gal80; CPR
G02	G01	pgRNA-int16-int17, int16::pSeGal2-CHI1, pSeGal2-CHR1, pSeGal2-CHS1, int17::pSptGal2-PAL1, pSptGal2-StsTAL, pSkGal1-C4H1, pSkGal10-4CL1	Liquiritigenin (**2**)
G03	G02	pgRNA-int5, int5::pSmGal2-IFS1, pSbGal2-HID1, pSmGal2-OMT1	Formononetin (**5**)
G04	G03	pgRNA-int21, int21::pSpdGal2-IFR1, pScGal2-I2'H1, pScGal2-VR1, pSeGal2-PTS1	Meidcarpin (**8**)
G05	G04	pgRNA-int6, int6::pSeGal2-OC1, pSeGal2-PTR1, pSpdGal2-PT1, pDDI2-DMT1, rDNA::pPGK1-Hyg, pSeGal2-ScIDI1, pSeGal2-RpHMGR	4'-*O*-methylgalbridin(**11**), Galbridin (**15**)
G06	G05	pgRNA-P_{ERG20}, ERG20::pHXT1-ERG20	4'-*O*-methylgalbridin(**11**), Galbridin (**15**)
G07	G06	pgRNA-int7, int7::pSeGal2-ZWF1, pSeGal2-IDP2	4'-*O*-methylgalbridin(**11**), Galbridin (**15**)
T01	G01	pgRNA-int6, int6::pSeGal2-OC1, pSeGal2-PTR2, pSpdGal2-PcM4DT	PTR-PT-OC
T02	G01	pgRNA-int6, int6::pSeGal2-OC1, pSeGal2-PTR2, pSpdGal2-PcM4DT, pSeGal2-NhPDA1	PTR-PT-OC-DMT
T03	G01	pgRNA-int6, int6::pSeGal2-OC1, pSeGal2-PTR1, pSpdGal2-PT1, pSeGal2-NhPDA1	PTR-PT-OC-DMT(NhPDA1)
T04	G01	pgRNA-int6, int6::pSeGal2-OC1, pSeGal2-PTR1, pSpdGal2-PT1, pSeGal2-DMT1	PTR-PT-OC-DMT(GgDMT1)
T05	G01	pgRNA-int6, int6::pSeGal2-OC1, pSeGal2-PTR1, pSpdGal2-PT1, pDDI2-DMT1	PTR-PT-OC-DMT(pDDI2-GgDMT1)

Supplementary Table 9. Model parameters.

Type	Parameters	Note
E	0.01	[1]
total_time	5	[2]
Kcat1/Km1	27759.76	[3]
Kcat2/Km2	247.15	
Kcat3/Km3	45.403	
Kcat4/Km4	0	
Kcat5/Km5	1560.609	[4]
Kcat6/Km6	841.56	
Kcat7/Km7	2136.63	
Kcat8/Km8	25359.33	
Kcat9/Km9	131.52	
Kcat10/Km10	23.4326	
Km1	0.012879	[5]
Km2	0.015469	
Km3	0.029892	
Km4	0.006635	
Km5	0.004527	
Km6	0.005523	
Km7	0.006004	
Km8	0.012721	
Km9	0.01717	
Km10	0.03298	
K8	0/100	[6]
K9	46.59/53.41	
K10	8.174/91.826	
K11	0/100	
K12	0/100	
K13	88.43/11.57	
K14	26.5/73.5	
K15	0/100	
rate	2	[7]
time_ratio	0	[8]

[1] total enzyme
[2] days
[3] *Kcat/Km* data of reaction 1, data below are defined similarly
[4] the value / 10 for theNhDMT1, and keep original for GgDMT1, same for *Kcat5~Kcat7*
[5] *Km* data of reaction 1, data below are defined similarly
[6] the ratio of compound 8: extracellular / intracellular, ratio below are defined similarly
[7] rate at which compounds enter and exit cells
[8] DMT induced time out of total fermentation time, time_ratio is in the range of [0:1), when time_ratio is 0, it means that DMT is constitutive expression

Supplementary references

1 Liu, T. et al. Construction of ajmalicine and sanguinarine *de novo* biosynthetic pathways using stable integration sites in yeast. *Biotechnol. Bioeng*. **119**, 1314–1326 (2022).

2 Shaw, W. M., Khalil, A. S. & Ellis, T. A multiplex MoClo toolkit for extensive and flexible engineering of *Saccharomyces cerevisiae*. *ACS Synth. Biol.* **12**, 3393–3405 (2023).